

www.acsnano.org

Wavelength Tunable Infrared Perfect Absorption in Plasmonic Nanocrystal Monolayers

Woo Je Chang, Zarko Sakotic, Alexander Ware, Allison M. Green, Benjamin J. Roman, Kihoon Kim, Thomas M. Truskett, Daniel Wasserman, and Delia J. Milliron



Cite This: ACS Nano 2024, 18, 972-982



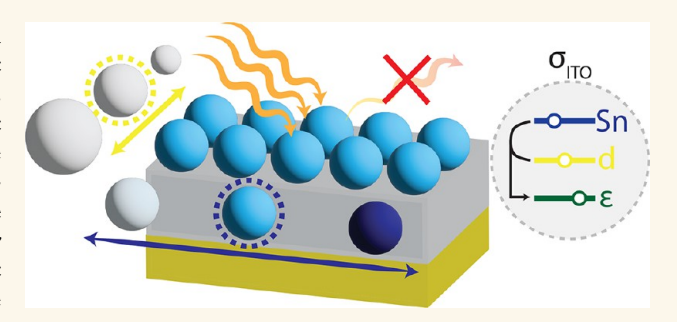
ACCESS

Metrics & More

Article Recommendations

s Supporting Information

ABSTRACT: The ability to efficiently absorb light in ultrathin (subwavelength) layers is essential for modern electro-optic devices, including detectors, sensors, and nonlinear modulators. Tailoring these ultrathin films' spectral, spatial, and polarimetric properties is highly desirable for many, if not all, of the above applications. Doing so, however, often requires costly lithographic techniques or exotic materials, limiting scalability. Here we propose, demonstrate, and analyze a mid-infrared absorber architecture leveraging monolayer films of nanoplasmonic colloidal tin-doped indium oxide nanocrystals (ITO NCs). We fabricate a series of ITO NC monolayer films using the liquid—air



interface method; by synthetically varying the Sn dopant concentration in the NCs, we achieve spectrally selective perfect absorption tunable between wavelengths of two and five micrometers. We achieve monolayer thickness-controlled coupling strength tuning by varying NC size, allowing access to different coupling regimes. Furthermore, we synthesize a bilayer film that enables broadband absorption covering the entire midwave IR region ($\lambda = 3-5 \mu m$). We demonstrate a scalable platform, with perfect absorption in monolayer films only hundredths of a wavelength in thickness, enabling strong light-matter interaction, with potential applications for molecular detection and ultrafast nonlinear optical applications.

KEYWORDS: localized surface plasmon resonance, indium tin oxide, infrared, perfect absorption, thin absorber, transparent conducting oxide

ngineering "perfect" absorption (PA) of infrared (IR) light is of fundamental and practical interest, partic- \checkmark ularly in the mid-IR region (3–30 μ m). This region hosts the spectral signatures of molecular vibrations, contains the midwave IR (MWIR) and long-wave IR (LWIR) atmospheric transparency windows (3-5 and 8-12 μ m, respectively), and coincides with thermal emission peaks of room temperature and hot objects. Infrared perfect absorbers can serve as vital components in optical and optoelectronic applications such as photodetection, 1,2 thermal emission engineering,³⁻⁶ and sensing.^{7,8} Considerable attention has been devoted to realizing ultrathin perfect absorbers, 9,10 driven by the dual benefits of reducing device volume and offering enhanced efficiency and sensitivity. Confining the absorption process to deeply subwavelength scales has proven beneficial for single photon detection 11,12 and quantum transduction, 13 as well as for exploring ultrafast nonlinearities for switching 14 and laser mode-locking.15

Most ultrathin absorber demonstrations so far were based on patterned metamaterials, thin-film metal, doped semiconduc-

tor, and phononic layers, ^{10,16,17} and more recently 2D materials such as graphene and transition metal dichalcogenides. ¹⁸ Lithographically patterned metamaterials have been particularly successful at enabling spectrally flexible and functional perfect absorbers ¹⁹ due to their ability to control the amplitude, phase, wavelength, and polarization of light. However, the reliance on expensive, high-resolution nanopatterning techniques can be a limiting factor in their scalability. ^{19–23} Similarly, 2D materials have shown great promise for efficient light absorption and detection, ^{18,24} but also suffer from limited scalability due to challenging growth and transfer processes involved in their photonic integration.

Received: October 8, 2023
Revised: December 10, 2023
Accepted: December 14, 2023
Published: December 20, 2023





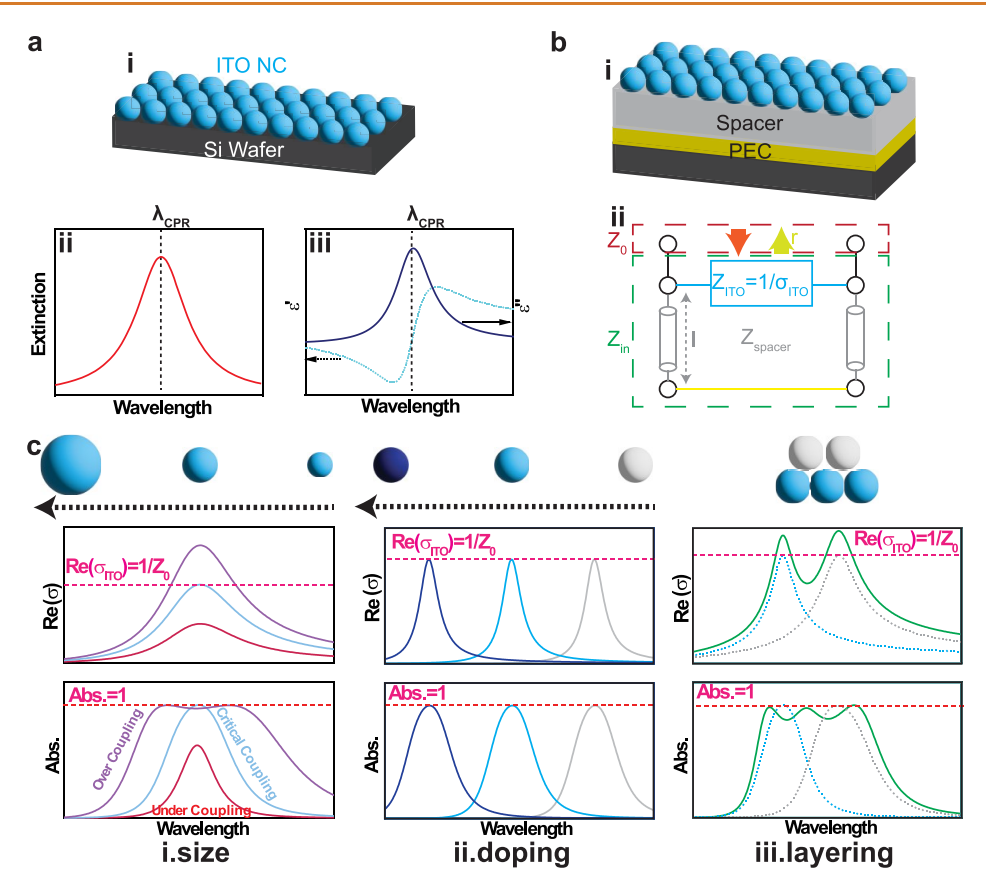


Figure 1. Design principle of our perfect absorber based on the impedance matching process. (a) Schematic of an ITO NC monolayer structure on a Si wafer with representative (i) extinction and (ii) complex permittivity spectra (iii) The permittivity line shape for NC monolayer on a Si wafer. (b) (i) Schematic of the perfect absorber structure and (ii) its equivalent transmission line circuit. Effective conductivity is tunable through the control of (c) (i) NC size, (ii) Sn doping, and (iii) the layering of two different types of ITO NCs. The expected absorption spectra are shown schematically below.

Moreover, most 2D absorber designs either rely on intrinsically invariant material (excitonic and phononic) resonances (which limits their spectral flexibility), or again, require broad-area lithographic patterning to engineer absorbing resonances.

Recently, a material-agnostic framework has been developed for analytically determining the minimal material thickness capable of exhibiting PA.²⁵ While that study envisioned thin film materials with resonant absorptive response, the same framework applies to any lossy thin film, including metamaterials with engineered resonant response. Using a highly reflective (perfect electrical conductor, or PEC) backplane with a quarter-wave spacer layer, or alternatively, a perfect magnetic conductor (PMC) backplane with negligible spacer layer, PA in layers only nanometers thick was predicted for a range of real world materials (AlN, hBN, SiC, GaAs, etc). Interestingly, at these ultrathin dimensions, only the imaginary part of the permittivity determines the minimal thickness at which the thin film can absorb all incident light. This framework could be especially useful for thin films whose resonant absorption response, i.e., effective imaginary permittivity, can be engineered to enable the design of a wavelength-flexible architecture capable of PA in ultrasubwavelength layers.

In that context, colloidal plasmonic nanocrystals (NCs) offer a potentially ideal material system for the demonstration of scalable ultrathin perfect absorbers. The NCs can serve as meta-atoms with broadly tunable extinction features, which can further form large-area metamaterials with engineered resonant

absorption. Noble metal NCs are suitable absorbers at the visible wavelengths. ^{26,27} However, at long wavelengths, the large, negative permittivity of conventional metals precludes a localized plasmonic response in subdiffraction-limit nanoparticles. ³⁰ For larger metallic NCs, mid-IR resonant response is achievable only by stacking multiple layers of NCs. ^{31,32} This stacking process makes the absorber layer thickness close to the μ m scale, precluding the realization of the benefits of a thin perfect absorber.

Unlike conventional metallic NCs, doped metal oxide NCs exhibit a frequency-tunable localized surface plasmon resonance (LSPR) that is influenced not only by the NC size but also, primarily, by the dopant concentration incorporated during synthesis. This feature weakens the linkage between NC size and resonance wavelength, offering a more systematic (and more flexible) approach to metamaterial design leveraging NCs as meta-atoms. Moreover, a single metal oxide NC, even below 10 nm in diameter, can exhibit a resonance wavelength in the mid-IR, which has enabled efficient optical switching of IR light 36-38 and the demonstration of molecular sensors using such NCs to enhance molecular vibrational signals.³⁹ The transparency of metal oxide NCs to visible light also ensures that their presence does not compromise any visible light response, making them suitable for thermal absorbers in sunlight management.⁴⁰ We recently showed that the tin-doped indium oxide (ITO) NCs can form a compact monolayer where NCs couple strongly to each other, giving rise to a collective plasmon response

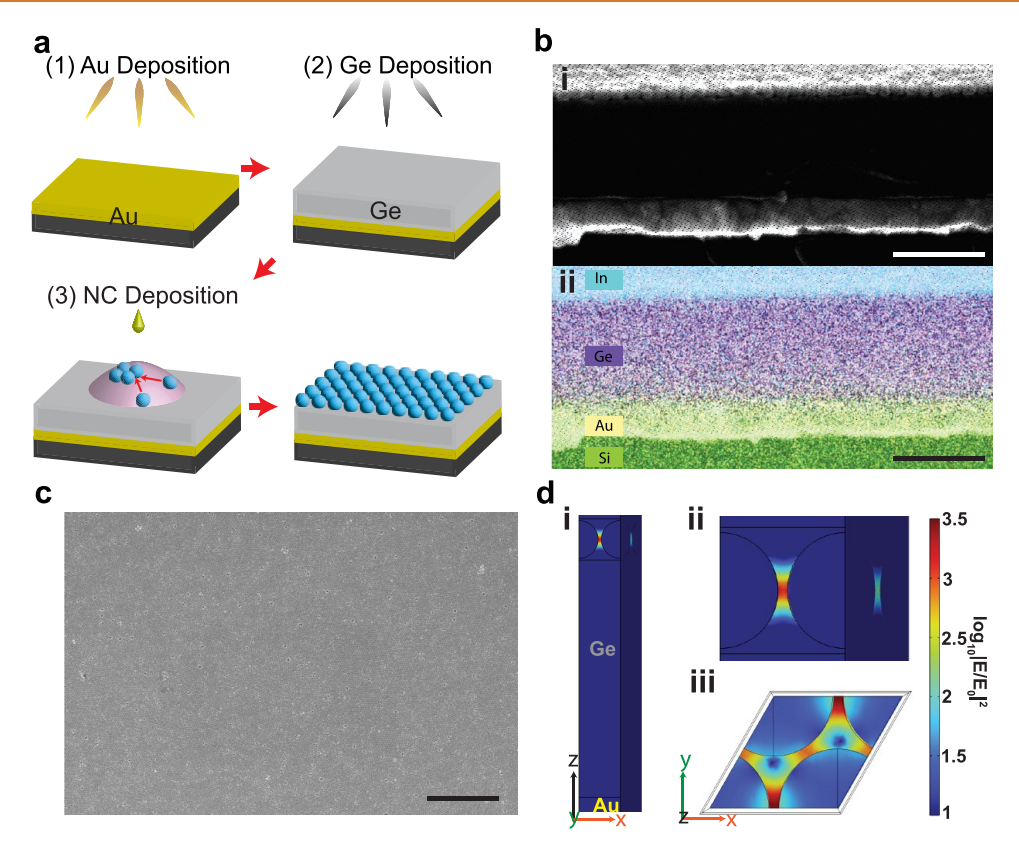


Figure 2. Structure of ITO NC-based perfect absorber. (a) Fabrication process of a perfect absorber. (b-i) Cross-sectional SEM of the perfect absorber with 6% Sn doped ITO NCs having 28 nm diameter. (b-ii) EDS elemental mapping of the cross-sectional SEM (scale bar 200 nm). (c) Top-down SEM of the ITO NC monolayer (scale bar $1\,\mu$ m), which is an identical sample from (b). (d) Electric field distribution at 3.1 μ m calculated using FEM simulations. Our model includes a 3% Sn-doped 31 nm ITO NC monolayer as an absorbing layer, a 195 nm Ge spacer layer, and a 78 nm Au layer below the spacer. We consider light that is normally incident (along the z-axis) and polarized along the x direction. (i) A cross-section map throughout the x-z plane, (ii) a magnified map of (i) focused on the NC region, and (iii) a cross-section map throughout the x-y plane.

(CPR).⁴¹ The NC monolayer was shown to effectively act as a mid-IR metasurface with frequency-tunable reflection, absorption, and epsilon near zero (ENZ) properties.⁴¹ In that study, the tunable resonant frequency of the ITO NCs made them versatile meta-atoms, where the effective properties of the optical layer could be varied by incorporating ITO NCs with two different Sn concentrations (and therefore different LSPR frequencies) within a single monolayer.

Here, we demonstrate the capability of tailoring mid-IR absorption properties using ITO NC assemblies. We predict, design, and experimentally validate PA in a series of ultrathin monolayer samples. We demonstrate control over the MWIR absorption features' strength, spectral position, and bandwidth by judiciously controlling the size and doping of NCs and combining two monolayers in a single photonic cavity. We show spectrally selective perfect absorbers tunable between 2 and 5 μ m and thickness-controlled coupling strength between the photonic and CPR resonances at a single wavelength. We also show that layering different ITO NCs can significantly broaden the CPR, resulting in a broadband strong absorption feature covering the whole MWIR band. The demonstrated perfect absorber is tunable across the mid-IR, lithography-free, and largely insensitive to polarization and angle, while the absorption process is confined to thicknesses less than a hundredth of the operating wavelength. These properties make the ITO NC-based perfect absorbers a promising system for IR sensing and detection schemes and for ultrafast nonlinear phenomena and switching.

RESULTS AND DISCUSSION

Design Principle and Fabrication Process. Closepacked monolayer films of ITO NCs exhibit a resonant peak in their optical extinction spectra and associated effective complex permittivity similar to other resonantly absorbing materials, as shown schematically in Figure 1a. As shown previously, 41 ITO NC monolayer films have a distinct extinction peak [Figure 1a (ii)], which is associated with the CPR of the NC array (at λ_{CPR}). Due to the dense packing and uniformity of the monolayer film, its optical properties are well represented by an effective complex permittivity with a finite width, resonant absorption feature, centered at the peak wavelength of the CPR of the NC array, as shown in Figure 1a (iii). According to our recent theoretical work, ²⁵ such films are ideally suited for the design of perfect absorbers at the ultrathin limit, when integrated with simple optical cavities. To that end, our design uses a classic Fabry-Pérot cavity absorber in the Salisbury screen configuration, 42,43 where a thin lossy film, in our case, the ITO NC film, is placed on top of a quarter-wave lossless dielectric spacer, which is backed by a PEC, as illustrated in Figure 1b(i). To analytically describe the absorbing properties of the proposed structure and to introduce our design principle, we employ transmission line theory and impedance matching arguments,44 representing the

structure with an equivalent transmission line model as shown in Figure 1b(ii). Due to its deep subwavelength thickness (a single NC diameter, consistent with our previous work),⁴¹ the ITO NC monolayer, in our transmission line formalism, can be treated as a planar sheet with an effective conductivity:⁴⁵

$$\sigma_{\rm ITO} = \frac{1}{Z_{\rm ITO}} = \frac{1}{Z_0} \frac{-i2\pi(\varepsilon_{\rm eff}(\lambda) - 1)t}{\lambda} \tag{1}$$

where σ_{ITO} is the sheet conductivity of the ITO NC monolayer, $\varepsilon_{\text{eff}} = \varepsilon' + \mathrm{i}\varepsilon''$ is the complex effective permittivity of the NC film [Figure 1b(iii)], t is the monolayer thickness (equivalent to the NC diameter), λ is the free-space wavelength of the incident light, and Z_0 and Z_{ITO} are free-space and effective NC monolayer impedances, respectively. The resonant absorption (associated with ε'' of the NC monolayer) corresponds to a resonant real conductivity (eq 1), as schematically shown in Figure 1b(ii). The reflection coefficient of the idealized structure from Figure 1a goes to zero, i.e., the structure perfectly absorbs all incoming light, when the real part of the ITO conductivity is equal to the characteristic admittance of air (inverse free-space impedance, i.e., identical to impedance-matching with air - see the Supporting Information, SI):

$$Re(\sigma_{\rm ITO}) = \frac{1}{Z_0} \frac{2\pi \varepsilon'' t}{\lambda} = \frac{1}{Z_0}$$
 (2)

The spacer thickness is optimized to induce destructive interference for outgoing waves. In the ultrathin regime, as indicated by eq 2, the film's conductivity depends linearly on both thickness and the imaginary part of the effective permittivity - properties which ITO NC monolayers are particularly well suited for controlling, as we next show. Since we use ultrathin NC films, the critical conductivity value requires a large ε'' , which is reached at or near λ_{CPR} , as shown in Figure 1c where the critical conductivity value, $Re(\sigma) = 1/Z_0$, is shown as a dashed line. Equation 2 can immediately predict whether a given ITO NC monolayer can exhibit PA in this cavity architecture; for example, for 3.5 μ m light and 31 nm NC diameter, the PA condition requires $\varepsilon'' \sim 17$, which is easily achievable with previously demonstrated ε_{eff} at λ_{CPR} in ITO NC monolayers.

Our concept for a perfect absorber platform (outlined in Figure 1c) leverages the ability to vary size [Figure 1c(i)] and the Sn doping concentration [Figure 1c(ii)] of the ITO NCs to enable independent tuning of the CPR spectral position and strength (as a result of changing LSPR characteristics of the NCs), which both influence the film's effective conductivity. In turn, we can tune both the strength and spectral position of the absorption feature of the photonic system [Figure 1c(i-ii)]. As a result, the cavity can be tailored to be under-coupled, critically coupled, or overcoupled, all at a chosen wavelength, based on the $Re(\sigma)$ peak value relative to $1/Z_0$. The predicted coupling regime informs expectations of the potential to achieve PA and the spectral line shape (Figure 1c). Furthermore, ITO NCs are conducive to layering, enabling films that combine NCs with different CPR spectral positions [Figure 1c(iii)]. Combining spectrally distinct CPRs can result in significant broadening of the absorption, thus enabling control not only over coupling strength and spectral position of absorption, but also over its bandwidth, all by straightforward self-assembly of the plasmonic absorber layer.

To realize the configuration we conceptualized, we deposited 78 nm of gold on a silicon substrate to serve as a PEC (Figure 2a); in the long wavelengths of the mid-IR, the large negative permittivity of the noble metals allows them to effectively be treated as PECs. Subsequently, we grew the Ge layer as a spacer for the cavity structure with a thickness determined by the CPR wavelength of the ITO NC monolayer to be deposited. ITO NCs were synthesized with an established slow injection method where the Sn dopant concentration is controlled by the mixing ratio of Sn and In in the precursor solution and the size is determined by the volume of precursor solution injected in the reaction flask.³³ Synthesized ITO NC size and size uniformity were analyzed by bright field scanning transmission electron microscopy (Figure S3) and dopant concentrations were measured by inductively coupled plasma-mass spectrometry of acid-digested NCs (Table S1). To integrate the NCs with the photonic cavity, we placed a water droplet on top of the Ge spacer, then dispensed a droplet containing oleate-capped ITO NCs (dispersed in 2:1 hexane:toluene) on top. As we previously reported, 41,46 slow evaporation of the solvent produces a compact monolayer of ITO NCs (Figure 2a). Although Akselrod et al. 47 showed that isolated NCs on the top of a spacer-PEC geometry can exhibit perfect absorption behavior, close-packed layers of NCs increase their extinction 41,48 (and thus, the imaginary part of permittivity) due to the collective plasmon coupling behavior. In addition, a close-packed NC structure enables the creation of a high density of plasmonic hot spots, which can enhance the light-matter interaction, sensing,⁵⁰ or optical switching applications.³⁸

Cross-sectional scanning electron microscopy (SEM) and compositional mapping by energy dispersive spectroscopy (EDS) confirm the uniformity and intended thickness of each layer [Figure 2b,c]. The uniformity of the ITO NC film over a large area allows us to model this monolayer as a planar slab with an effective sheet impedance. To visualize the electric field distribution in the perfect absorber, we modeled the optical stack, including an ITO NC monolayer (with parameters consistent with 3% Sn doped ITO NCs, namely $\omega_v = 12541$ cm⁻¹ and $\gamma_p = 672$ cm⁻¹), a 195 nm thick Ge spacer layer, and an underlying 78 nm layer of gold using the finite element method (FEM) as shown in Figures S1 and S2. For resonant excitation at normal incidence, we observe a strong enhancement of the electric field within the monolayer of ITO NCs, specifically concentrated in the gaps between the NCs (Figure 2d and Figure S2), promoting the strong absorption observed in our system.

Size and Doping Variation on ITO NCs and Following Absorption Behavior. The ability to control light-matter interaction strength is of broad interest to polaritonic physics and chemistry. 51,52 Specifically, tuning between undercoupled, critically coupled, and overcoupled regimes is an important characteristic of ultrathin absorbers. 53,54 ITO NCs enable tuning of the coupling strength by varying the NC size, i.e., monolayer thickness [Figure 1c(i)]. To study the effect of monolayer thickness on the reflection spectra, we synthesized ITO NCs with diameters of 12, 17, 25, and 31 nm (Figure S3). The LSPR wavelength of dispersed ITO NCs depends primarily on Sn doping concentration and is nearly sizeinvariant in this diameter range. 55 However, in the closepacked monolayers the NC spacing is approximately constant, determined by the steric bulk of the oleate ligands. As such, larger NCs are packed more densely, resulting in a larger

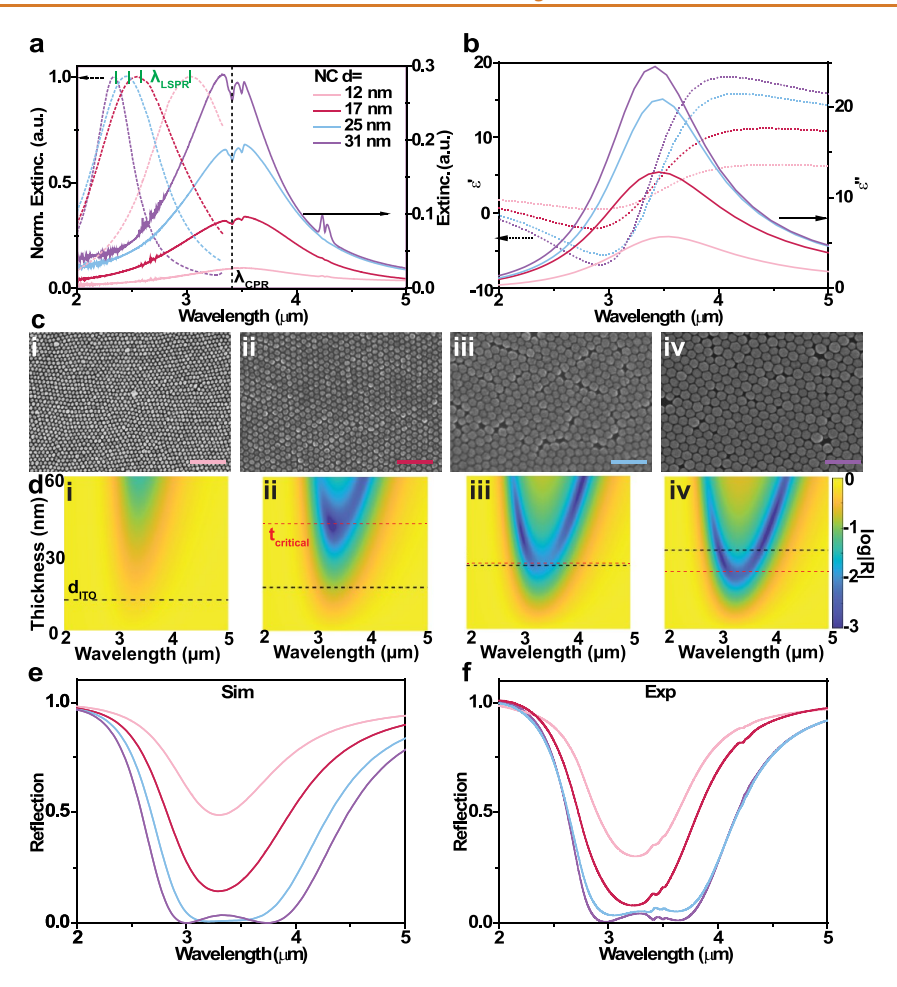


Figure 3. NC size-dependent light absorption behavior at fixed resonant wavelength. (a) Extinction spectra for solvent dispersions (dashed) and monolayers of ITO NCs on Si substrates (solid). The solution phase spectra (in tetrachloroethylene) are normalized for clarity. (b) Complex effective permittivity of each ITO NC monolayer derived using MPM. (c) SEM of ITO NC monolayers with (i) 12, (ii) 17, (iii) 25, and (iv) 31 nm ITO NCs. All scale bars are 100 nm. (d) Calculated reflection spectra as a function of monolayer thickness and wavelength (log scale) for $d_{\text{ITO}} = \text{(i)} 12$, (ii) 17, (iii) 25, and (iv) 31 nm ITO NCs. t_{critical} are depicted with red dashed lines. t_{critical} for (i) is 95 nm (not visible). (e) Simulated reflection spectra for each ITO NC monolayer [also designated as dashed lines in (d)]. (f) Measured reflection spectra for each ITO NC monolayer.

redshift in the resonance upon assembly. To compensate for this effect and achieve consistent CPR in the monolayers as we varied NC size, the Sn concentrations were fine-tuned to 2.2, 2.5, 2.7, and 3%, respectively, for increasing diameter. These adjustments caused the LSPR wavelengths of the solvent-dispersed NCs to vary systematically, being 3.0, 2.6, 2.4, and 2.3 $\mu \rm m$, respectively (Figure 3a). However, once the monolayers of each type of ITO NCs were formed, the CPR wavelengths converged to $\lambda_{\rm CPR}=3.4~\mu \rm m$. Thus, the synthetic tuning of the ITO NCs allows independent control over size and resonant wavelength in the assembled monolayers, which cannot be achieved with conventional metallic NCs. This control allowed us to interrogate different levels of effective loss and investigate different coupling regimes at a fixed wavelength using the same material.

To quantitatively understand the factors controlling the spectral shift from dispersions to monolayers, we characterized the spectra of the dispersed NCs by heterogeneous ensemble Drude approximation (HEDA) analysis (Figure S4). TO NCs are known to contain a plasmonic core with a high electron concentration, surrounded by a thin (few nm thick) near-surface depletion layer that reduces the LSPR coupling between neighboring NCs in a film. Fitting the LSPR spectra

of the solvent-dispersed NCs by HEDA analysis, we extracted the fraction of the NC volume occupied by its plasmonic core (and hence the depletion width) and the free electron concentration in that plasmonic region. Consistent with previously reported trends, we found that larger ITO NCs with higher Sn doping concentration have larger plasmonic core volume fractions, thinner estimated depletion widths, and higher charge carrier concentrations. All three of these factors favor stronger coupling, 46 so these electronic characteristics of the NCs explain the larger red-shift of LSPR wavelength upon monolayer formation for the bigger, more highly doped ITO NCs (Figure 3a).

Parameters obtained from HEDA fitting (Table S1) are also used to model the optical response of the NC monolayers and to predict spectra of the photonic devices. We derive the effective permittivity for monolayers of each NC type (varying doping and diameter) (Figure 3b), by applying the mutual polarization method (MPM) (details described in the SI). 41,46 We initially estimated the packing fractions to match experimental extinction spectra with MPM (Figure S5) and confirmed that these area fractions are consistent with those in the experimental samples by using threshold images from SEM (Figure S6). The in-plane component of the permittivity

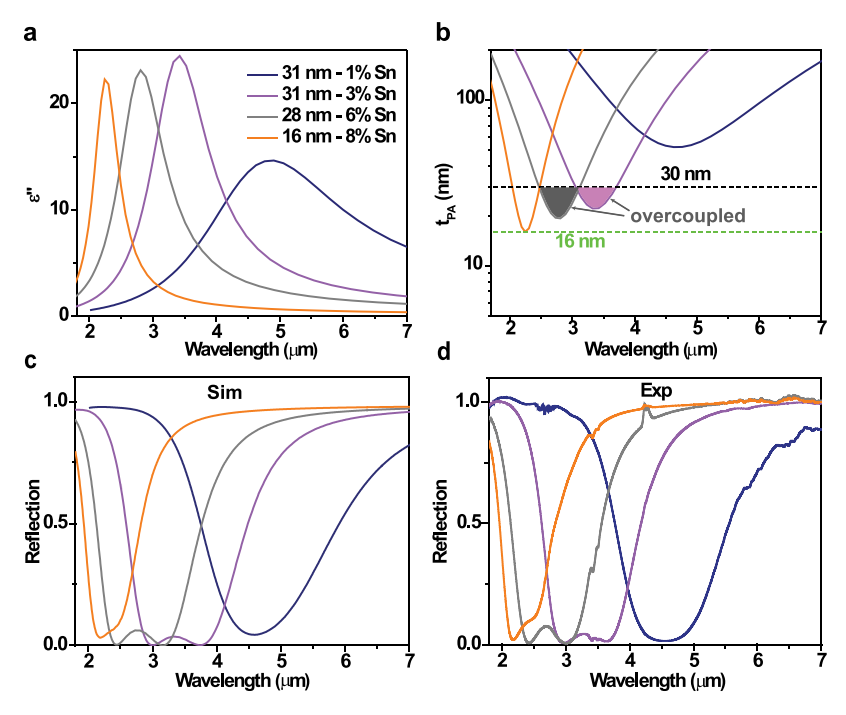


Figure 4. Wavelength tunability of perfect absorbers based on ITO NC monolayers. (a) Imaginary parts of the effective permittivity of NC monolayers calculated by MPM and (b) Calculated perfect absorption thickness condition for 28 nm NC with 6% Sn, 31 nm NC with 3% Sn, 31 nm NC with 1% Sn, and 16 nm NCs with 8% Sn assembled as monolayers. (c) Simulated and (d) experimental reflection spectra in the perfect absorber geometry.

computed by MPM is comparable to the permittivity extracted by fitting the normal incidence extinction spectra of NC monolayers on Si wafers, a conventional method for extracting permittivity from Lorentzian type oscillators (Figure S9). This agreement corroborates the accuracy of the MPM regarding the permittivity function (details in the SI).⁵⁸ The high uniformity of ITO NC monolayers, demonstrated for various NC diameters in Figure 3c(i-iv), all strongly subwavelength, enables the application of the sheet impedance model described in Figure 1 regardless of the ITO NC size.

Each ITO monolayer was modeled by its effective permittivity (Figure 3b), allowing us to simulate the reflection spectra of the total structure using the transfer matrix method (SI). To illustrate the effect of monolayer thickness (i.e., NC diameter) on the response of the structure, Figure 3d shows the contour plots of the simulated reflection spectra for the four samples as a function of monolayer thickness and wavelength. In the ultrathin regime, varying thickness is analogous to tuning conductivity (i.e., loss) according to eq 2, where each sample has a different critical thickness that marks the transition between undercoupled and overcoupled regimes. The critical thickness is calculated through eq 2 at resonance $(t_{critical})$ red dashed line in Figure 3d), while the value of the actual monolayer thickness (d_{ITO} , black dashed line in Figure 3d) relative to the critical thickness will determine the coupling regime, and ultimately, the spectral line shape. The smaller samples (12 and 17 nm diameter), Figure 3d(i-ii), are in the under-coupled regime ($d_{ITO} < t_{critical}$). Their reflection does not reach near-zero, and both exhibit a single reflection feature (Figure 3e). Simulated spectra for the 25 nm sample indicate that it lies close to the critical coupling regime ($d_{\rm ITO} \approx t_{\rm critical}$) with very low reflection values (absorption above 98% from 3.1 to 3.6 μ m), while the 31 nm sample shows obvious splitting of the reflection dips (positioned at 3 and 3.8 μ m), indicating that

this configuration is operating in the overcoupled regime (d_{ITO} $> t_{critical}$). Although overcoupling does not lead to perfect absorption directly at the CPR wavelength, overcoupling could be advantageous for molecular detection⁵⁹ and hot electron transfer schemes.⁶⁰ The experimental results (Figure 3f) closely match the simulated predictions, demonstrating the applicability of the model to these ITO NC-based metamaterials and the feasibility of using NC size to achieve thickness-controlled coupling strength. Simulated reflection spectra (Figure S10) using effective permittivities obtained from NC monolayer extinction spectra also closely match the experimental spectra (Figure 3f). The close matching with experimental results supports the usefulness of our theoretical framework described in eq 2 and further validates MPM for creating the effective permittivity functions of the NC monolayers. Finally, the reflection line shape of the 31 nm NC monolayer from Figure 3e also agrees with the reflection spectrum generated by the FEM (Figure S2), which supports the efficacy of our model in predicting the reflection spectra.

Since the CPR of ITO NC monolayers is tunable based on Sn concentration regardless of NC diameter, we can systematically study the coupling behavior at different resonance wavelengths for a fixed ITO NC diameter and demonstrate tunability of the perfect absorption feature across the mid-IR. NCs synthesized with 6, 3, and 1% Sn and around 30 nm diameter have $\lambda_{\rm LSPR}$ of 2.0, 2.3, and 3.3 μ m, respectively, in solvent dispersions (Figure S4). By forming monolayers of each of the ITO NCs on silicon substrates, the extinction spectra were measured and found to have $\lambda_{\rm CPR}$'s of 2.7, 3.3, and 4.5 μ m, respectively (Figure S5). Additionally, we prepared 8.0% Sn doped 16 nm ITO NCs, which have a $\lambda_{\rm CPR}$ of 2.3 μ m when assembled in a monolayer. Similar to the size series shown in Figure 3, the effective permittivity (Figure 4a and Figure S7) of each ITO NC monolayer was calculated with

MPM (details in the SI). By inserting the extracted wavelength-dependent imaginary part of the permittivity for each ITO NC monolayer into eq 2, we predicted the perfect absorption thickness for each case as $t_{\rm PA} = \lambda/2\pi\epsilon''(\lambda)$ (Figure 4b, also referred to as the resonant Woltersdorff thickness²⁵). This metric provides another way to visualize the impedance matching condition and predict the coupling regime between the cavity mode and the CPR. Considering the thickness of each of the ITO NC monolayers, we find that the 6, and 3% Sn ITO NC monolayers each match the perfect absorption thickness at two wavelengths, indicating that these layers are operating in the overcoupled regime. In contrast, the 1% Sn NC monolayer was slightly too thin to match the perfect absorption condition, suggesting slightly under-coupled behavior for this case. Lastly, the 8.0% Sn ITO NC monolayer closely matches the critical coupling condition (Figure 4b). Our experimental data (Figure 4d) agree well with these predictions, with two distinct dips reaching zero reflection observed for the 6 and 3% Sn ITO NC monolayers, one broad dip close to zero observed for the 1% ITO NC monolayer, and a broad near zero reflection feature observed for the 8% ITO NC monolayer (Figure 4b).

Targeting Angled and Broad Absorption. One important characteristic of a perfect absorber, for a number of potential applications, is achieving strong absorption across a wide solid angle, for both TE and TM-polarized incident light.4 We experimentally investigated the reflection of TMand TE-polarized light with a monolayer prepared with 3% Sn doped, 31 nm diameter ITO NCs in the photonic cavity structure described above. For TM-polarized light, we saw consistent near-perfect absorption up to incident angles of \sim 60° with respect to the normal (Figure 5a). We also observed a higher energy TM-polarized reflectance dip at 1.5 μ m, which grew stronger with increasing angle. For TE-polarized light, we observed a continuous decrease in absorption strength with increasing incidence angle (Figure 5c). To support our observations, we simulated the angle-dependent reflection spectra, taking into account the anisotropic nature of the effective permittivity, which we also calculated using MPM simulations (Figure S11).41 The TM-polarized reflectance simulation (Figure 5b) reproduces the observed, largely consistent, absorption until the angle reaches 60°, as well as the additional reflection dip observed around $\lambda \approx 1.5 \mu m$, which we ascribe to increasing excitation of the out-of-plane polarized mode (analogous to the Berreman mode for a homogeneous ITO slab). 61 The simulations also reproduced a progressive drop in absorption with increasing angle for TEpolarized light, similar to the experimental observations (Figure 5d). This trend is expected, as the structure shifts away from the perfect impedance matching condition at higher incidence angles. Overall, the structure maintains a broad angular bandwidth of strong absorption for both polarizations, as we can further corroborate from angle and wavelengthdependent contour maps (Figure S12) for each polarization.

Thus far, we have demonstrated tunable absorption features based on the synthetically controlled NC size and dopant concentration in the meta-atoms making up the monolayer films, all of which produced relatively narrow spectral absorption lineshapes. While high spectral selectivity is preferred in some applications, broadening the absorption band is highly desirable in others, e.g., for bolometric absorbing elements for thermal imaging applications⁶² or for thermal energy management,⁶³ both of which would benefit from

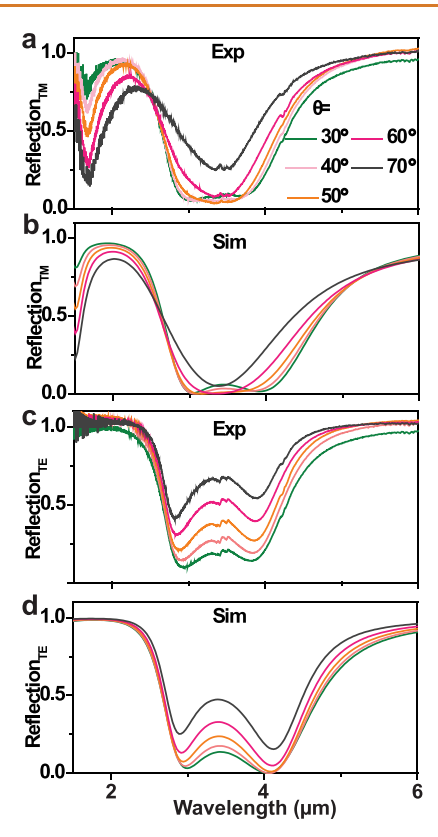


Figure 5. Angle dependent absorption behavior of 3% Sn doped 31 nm ITO NC monolayer. (a) Experimental and (b) simulated reflection spectra at oblique incidence angle for TM-polarized light. (c) Experimental and (d) simulated reflection spectra at oblique incidence angle for TE-polarized light.

broadband absorption across entire wavelength ranges such as the $3-5~\mu m$ MWIR atmospheric window. Previous attempts to broaden mid-IR absorption features for detectors often require rather complex multiresonant structures, ^{64,65} leaving room for the design of simpler and more scalable solutions. As we briefly introduced earlier [Figure 1c(iii))], our perfect absorber architecture can be extended to engineer spectral response by simply layering NCs having different synthetically controlled doping concentrations. By taking advantage of resonance tunability through doping, we design and demonstrate an absorber covering the whole MWIR range.

To integrate multiple NC layers in one structure, we modified the liquid-air assembly process by submerging the substrate with the fabricated cavity into an acetonitrile solution in a Teflon trough. Next, we deposited a small volume of the 3% Sn doped 31 nm NC solvent dispersion atop the acetonitrile subphase, allowing the NC monolayer to form at the air interface. After transferring the free-floating ITO NC film onto the substrate below by pipetting out the acetonitrile subphase, we repeated this procedure with 1% Sn doped 31 nm NC solvent dispersion to create a bilayer ITO NC film (Figure 6a). The extinction spectrum resulting from the bilayer deposition on a Si substrate shows two distinct extinction features at 3 and 4.2 μ m, which can be ascribed to contributions from the 3% and 1% Sn ITO NCs, respectively (Figure 6b). We use a two-layer optical model, where each layer's permittivity is modeled with a Lorentz resonance model (Figure S13), corresponding to 1% and 3% ITO monolayers, to fit the measured bilayer extinction spectra (Figure 6b). Using these effective permittivities, we designed and optimized

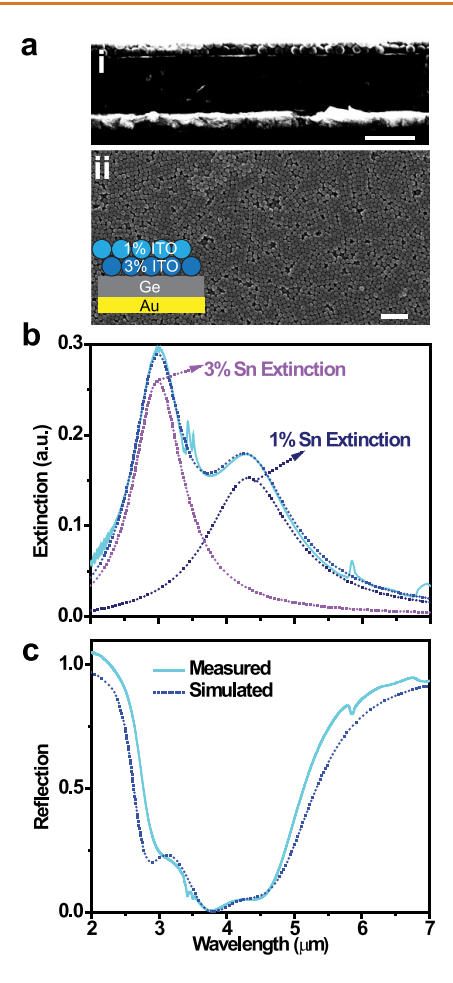


Figure 6. ITO NC bilayer based perfect absorber geometry and its reflection spectra. (a) (i) Cross-sectional and (ii) top-down SEM of NC bilayer perfect absorber structure (with schematic inset). All scale bars correspond to 200 nm. The 1% and 3% Sn 31 nm ITO NC layers are artificially colored blue and sky blue, respectively. (b) Extinction spectrum (solid line) of the NC bilayer on a Si wafer. We simulated two effective permittivity functions to accurately reproduce the extinction (dotted line) spectrum of the NC bilayer. (c) Measured and simulated reflection spectra of the ITO NC bilayer in the perfect absorber structure.

a cavity ($d_{\rm Ge}=200$ nm) with broadband absorption response, Figure 6c. The measured response displays near-impedance-matching conditions over a wide range of wavelengths—roughly 3–5 μ m—demonstrating an ultrathin wide-band absorber, with good agreement between the simulation and experiment. As shown in Figure S14 in the SI, varying the thickness can lead to perfect absorption at either CPR wavelength or at a single central perfect absorption point as shown in Figure 6c. However, Figure 6c demonstrates the broadest absorption spectra in general. Thus, this spacer thickness variation serves as another tunable parameter for our system to manipulate absorption.

CONCLUSION

We have demonstrated a photonic system with powerful control over its mid-IR absorption properties, realized in a scalable Salisbury screen configuration. By manipulating the synthetically controlled parameters of the ITO NCs, we have tuned the spectral position, strength, line shape, and bandwidth of the absorption features. Leveraging our analytical

model of the perfect absorber architecture, we are able to design, fabricate, and demonstrate wavelength flexible perfect absorption knowing only the permittivity of the monolayer of ITO NCs, which can be also simulated by MPM. These predictions find strong empirical support in our experimental results. Our NC-based perfect absorption platform allows highly customizable spectral response across a wide range of wavelengths owing to the potential for layering NC components, including ITO NCs with different doping concentrations and other NC compositions of interest.

We envision the application of our platform in the creation of frequency-tunable ultrafast optical modulators and nonlinear frequency-converters, both due to the ultrasubwavelength thickness, and due to the pronounced field localization in the ITO NC mono- or bilayers. Notably, the resonance of the ITO NC monolayers can be aligned with telecom band wavelengths, ³⁶ enabling all-optical switches for optical communications, ³⁸ where the reduced thickness of the perfectly absorbing monolayers could help enhance the speed and lower the power consumption of the switching process. Furthermore, the ultrathin nature and the transparency of our ITO NC layers to near IR and visible light suggests that high harmonics, which can be efficiently generated by mid-IR perfectly absorbing systems, would be able to effectively escape the material, 66 with potential applications to imaging⁶⁷ and quantum information On the other hand, the linear absorption processing. properties demonstrated already in this work are ideally suited for advanced detector design, with the significant advantage of wavelength output tuning in ultrathin layers offering benefits for applications such as bolometric detection. 62,69 In addition, we can potentially apply our platform for thermal control, such as thermal imaging⁷⁰ or thermal management devices⁷¹ that demand larger area (and low-cost) coverage for practical operation. The possibility of capacitive charging of the NC array, 72,73 which is more significant than that of thin films due to NC's large surface area, could also be applied to provide further in situ spectral modulation to these photonic systems.

EXPERIMENTAL SECTION

Materials. All chemicals were used without any purification step. Indium(III) acetate $[In(ac)_3, 99.99\%, Sigma-Aldrich]$, tin(IV) acetate $[Sn(ac)_4, Sigma-Aldrich]$, oleic acid (OA, 90%, technical grade, Sigma-Aldrich), oleyl alcohol (OLA, 90%, technical grade, Sigma-Aldrich), and octadecene (ODE, 85%, technical grade) were used to synthesize the NCs. Hexane (\geq 99.9%, Fischer Chemical) and toluene (99.8%, Sigma-Aldrich) were used for dispersing the NCs to form the monolayers.

Synthesis of ITO NCs. Nanocrystals were synthesized by established slow injection methods based on previous reports. 33,41 For 31 nm ITO NCs, we dissolved $8 \times (1-x)$ mmol of $\operatorname{In}(\operatorname{ac})_3$ and $8 \times x$ mmol of $\operatorname{Sn}(\operatorname{ac})_4$ in 16 mL of OA and 8 mL of ODE. x is based on the desired doping concentration. We then heated this solution to 160 °C under a nitrogen atmosphere for 2 h. In a separate flask, 13 mL of OLA was degassed under vacuum for 1 h at 140 °C. Then the OLA flask was heated to 290 °C under the nitrogen environment. Then using 50 mL of a glass syringe, we injected 21 mL of the metal precursor into the OLA solution with an injection rate of 0.3 mL min^{-1} by using a syringe pump. Once the injection was complete, we waited for an extra 20 min at 290 °C and started cooling until the mixture reached room temperature. Then we washed the solution with ethanol three times and redispersed it in 20 mL of hexane.

For 12, 17, and 25 nm ITO NCs, we dissolved $0.5 \times (1-x)$ mol L⁻¹ of $In(ac)_3$ and $0.5 \times x$ mol L⁻¹ of $Sn(ac)_4$ in OA and put in under vacuum for 1 h at 100 °C. We then heated this precursor up to 150 °C for 2 h under the nitrogen. We then prepared 13 mL of OLA

under nitrogen atmosphere at 290 °C. We then slowly injected the metal precursor solution with 0.35 mL min⁻¹ at 290 °C using a glass syringe and a syringe pump. *x* values for 12, 17, and 25 nm ITO NCs are 0.018, 0.022, and 0.028, respectively. The volumes of injected metal precursor for 12, 17, and 25 nm ITO NCs are 4.5, 12, and 25 mL, respectively. For 25 nm ITO NC, after injecting 10 mL of metal precursor, we stopped the metal precursor injection and started the injection of OLA at the rate of 0.2 mL min⁻¹. We repeated OLA injection step one more time after we added an extra 10 mL of metal precursor injection. We then injected 5 mL of leftover metal precursor solution. Synthesized NCs dispersed in OA or OA/ODE solution are centrifuged with an excess amount of ethanol after diluting the NC dispersions with hexane. The washed NCs are redispersed in hexane.

ito NC characterization. As-synthesized ITO NCs and monolayers of ITO NCs were imaged using a Hitachi S5500 scanning transmission electron microscope (STEM) under the bright field STEM and secondary electron (SE) modes, respectively. The extinction spectra of the solvent-dispersed NCs were measured with a Bruker Vertex 70 Fourier transform infrared (FTIR) spectrometer in a transmission configuration with a 1 cm beam diameter holder. For the inductively coupled plasma mass spectrometry (ICP-MS), we first dried the ITO NC solution and added aqua regia for digestion. After 2 days of digestion, we diluted this solution to 2% nitric acid and utilized an Agilent 7500ce spectrometer to measure the concentration of each element.

Device Fabrication. We sequentially deposited a 9 nm chromium (Cr) adhesion layer, 78 nm of Au, and Ge dielectric spacer by e-beam evaporation onto silicon substrates. The ITO NC monolayer preparation was carried out as described in our previous work.4 We then dropped water onto the substrate and sequentially dropped a 1 mg mL⁻¹ ITO NC dispersion (hexane:toluene = 2:1 by volume) on top of the water droplet. We used a glass slide to control the evaporation rate of organic solvent. Then we uncovered the sample to evaporate the water, leaving the NC monolayer resting on the Ge spacer layer. For NC bilayer formation, we first put the substrate in a Teflon well and added 5 mL of acetonitrile. We then drop casted 35 μL of ITO NC solution (3 mg mL⁻¹) onto the acetonitrile subphase, where the monolayer of ITO NC is formed within 10 s. After draining the acetonitrile subphase, the monolayer NC film was transferred onto the substrate. We iterate this procedure again to make a bilayer of ITO NCs. For extinction spectra of the NC monolayer, we did the same procedure on double-side polished undoped silicon wafers.

Device Measurement. The main experimental reflection measurements were obtained using an IR microscope (Bruker Hyperion 2000) with a Cassegrain objective, attached to a Bruker Vertex V70 FTIR. The input light polarization was mixed, while collected light is slightly angled off of normal incidence, and there is a small angular spread due to the presence of Cassegrain. When simulating the reflection coefficient, the angular spread can be disregarded due to the weak angular dispersion at small angles of the ITO monolayers. The angle-dependent reflection measurement was conducted using a Bruker Vertex 70 FTIR with a VeeMax III angle-dependent reflection spectroscopy tool from Pike Industries. The polarization of the incident light was controlled with a wire-grid polarizer in the FTIR beam path. For all reflection spectroscopy measurements, a gold-coated substrate, providing near-perfect reflection in the MWIR, served as a reference.

ASSOCIATED CONTENT

Data Availability Statement

The data supporting the findings of both the manuscript and its preprint version ⁷⁴ are available upon a reasonable request from the corresponding authors.

Supporting Information

The Supporting Information is available free of charge at https://pubs.acs.org/doi/10.1021/acsnano.3c09772.

Details for materials, HEDA, MPM, fitting-based permittivity, angle-dependent spectra, and layer-dependent simulation details (PDF)

AUTHOR INFORMATION

Corresponding Authors

Thomas M. Truskett — McKetta Department of Chemical Engineering, University of Texas at Austin, Austin, Texas 78712, United States; Department of Physics, University of Texas at Austin, Austin, Texas 78712, United States; orcid.org/0000-0002-6607-6468; Email: truskett@che.utexas.edu

Daniel Wasserman — Chandra Family Department of Electrical and Computer Engineering, University of Texas at Austin, Austin, Texas 78758, United States; orcid.org/ 0000-0003-3234-0803; Email: dw@utexas.edu

Delia J. Milliron — McKetta Department of Chemical Engineering, University of Texas at Austin, Austin, Texas 78712, United States; Orcid.org/0000-0002-8737-451X; Email: milliron@che.utexas.edu

Authors

Woo Je Chang – McKetta Department of Chemical Engineering, University of Texas at Austin, Austin, Texas 78712, United States; oorcid.org/0000-0003-0796-9271

Zarko Sakotic — Chandra Family Department of Electrical and Computer Engineering, University of Texas at Austin, Austin, Texas 78758, United States; orcid.org/0000-0003-3886-1378

Alexander Ware — Chandra Family Department of Electrical and Computer Engineering, University of Texas at Austin, Austin, Texas 78758, United States; ocid.org/0009-0002-5693-7727

Allison M. Green – McKetta Department of Chemical Engineering, University of Texas at Austin, Austin, Texas 78712, United States; ⊙ orcid.org/0000-0002-7734-4202

Benjamin J. Roman — McKetta Department of Chemical Engineering, University of Texas at Austin, Austin, Texas 78712, United States; © orcid.org/0000-0003-2213-2533

Kihoon Kim — McKetta Department of Chemical Engineering, University of Texas at Austin, Austin, Texas 78712, United States; oocid.org/0000-0003-1034-9233

Complete contact information is available at: https://pubs.acs.org/10.1021/acsnano.3c09772

Author Contributions

*These authors contributed equally to this work

Notes

The authors declare no competing financial interest.

ACKNOWLEDGMENTS

This work was primarily supported by the National Science Foundation through the Center for Dynamics and Control of Materials: an NSF MRSEC under Cooperative Agreement Nos. DMR-1720595 and DMR-2308817, with additional support from the Welch Foundation (F-1696 and F-1848). Z.S and D.W. acknowledge support from the Defense Advanced Research Projects Agency (DARPA) under the Optomechanical Thermal Imaging (OpTIm) program (HR00112320022).

REFERENCES

- (1) Landy, N. I.; Sajuyigbe, S.; Mock, J. J.; Smith, D. R.; Padilla, W. J. Perfect metamaterial absorber. *Phys. Rev. Lett.* **2008**, *100*, 207402.
- (2) Li, W.; Valentine, J. Metamaterial perfect absorber based hot electron photodetection. *Nano Lett.* **2014**, *14*, 3510–3514.
- (3) Greffet, J.-J.; Carminati, R.; Joulain, K.; Mulet, J.-P.; Mainguy, S.; Chen, Y. Coherent emission of light by thermal sources. *Nature* **2002**, *416*, 61–64.
- (4) Diem, M.; Koschny, T.; Soukoulis, C. M. Wide-angle perfect absorber/thermal emitter in the terahertz regime. *Phys. Rev. B* **2009**, 79, 033101.
- (5) Streyer, W.; Law, S.; Rooney, G.; Jacobs, T.; Wasserman, D. Strong absorption and selective emission from engineered metals with dielectric coatings. *Opt. Express* **2013**, *21*, 9113–9122.
- (6) Mason, J. A.; Smith, S.; Wasserman, D. Strong absorption and selective thermal emission from a midinfrared metamaterial. *Appl. Phys. Lett.* **2011**, *98*, 241105.
- (7) Liu, N.; Mesch, M.; Weiss, T.; Hentschel, M.; Giessen, H. Infrared perfect absorber and its application as plasmonic sensor. *Nano Lett.* **2010**, *10*, 2342–2348.
- (8) Mason, J. A.; Allen, G.; Podolskiy, V. A.; Wasserman, D. Strong Coupling of Molecular and Mid-Infrared Perfect Absorber Resonances. *IEEE Photonics Technol. Lett.* **2012**, 24, 31–33.
- (9) Ra'di, Y.; Simovski, C. R.; Tretyakov, S. A. Thin perfect absorbers for electromagnetic waves: theory, design, and realizations. *Phys. Rev. Appl.* **2015**, *3*, 037001.
- (10) Kats, M. A.; Capasso, F. Optical absorbers based on strong interference in ultra-thin films. *Laser Photonics Rev.* **2016**, *10*, 735–749.
- (11) Akhlaghi, M. K.; Schelew, E.; Young, J. F. Waveguide integrated superconducting single-photon detectors implemented as near-perfect absorbers of coherent radiation. *Nat. Commun.* **2015**, *6*, 8233.
- (12) Vetter, A.; Ferrari, S.; Rath, P.; Alaee, R.; Kahl, O.; Kovalyuk, V.; Diewald, S.; Goltsman, G. N.; Korneev, A.; Rockstuhl, C.; Pernice, W. H. P. Cavity-enhanced and ultrafast superconducting single-photon detectors. *Nano Lett.* **2016**, *16*, 7085–7092.
- (13) Kokkoniemi, R.; Girard, J.-P.; Hazra, D.; Laitinen, A.; Govenius, J.; Lake, R. E.; Sallinen, I.; Vesterinen, V.; Partanen, M.; Tan, J. Y.; Chan, K. W.; Tan, K. Y.; Hakonen, P.; Mottonen, M. Bolometer operating at the threshold for circuit quantum electrodynamics. *Nature* **2020**, *586*, 47–51.
- (14) Yang, Y.; Kelley, K.; Sachet, E.; Campione, S.; Luk, T. S.; Maria, J.-P.; Sinclair, M. B.; Brener, I. Femtosecond optical polarization switching using a cadmium oxide-based perfect absorber. *Nat. Photonics* **2017**, *11*, 390–395.
- (15) Wang, J.; Coillet, A.; Demichel, O.; Wang, Z.; Rego, D.; Bouhelier, A.; Grelu, P.; Cluzel, B. Saturable plasmonic metasurfaces for laser mode locking. *Light Sci. Appl.* **2020**, *9*, 50.
- (16) Ghobadi, A.; Hajian, H.; Butun, B.; Ozbay, E. Strong light-matter interaction in lithography-free planar metamaterial perfect absorbers. *ACS Photonics* **2018**, *5*, 4203–4221.
- (17) Nordin, L.; Dominguez, O.; Roberts, C.; Streyer, W.; Feng, K.; Fang, Z.; Podolskiy, V.; Hoffman, A.; Wasserman, D. Mid-infrared epsilon-near-zero modes in ultra-thin phononic films. *Appl. Phys. Lett.* **2017**, *111*, 091105 DOI: 10.1063/1.4996213.
- (18) Li, Q.; Lu, J.; Gupta, P.; Qiu, M. Engineering optical absorption in graphene and other 2D materials: advances and applications. *Adv. Opt. Mater.* **2019**, *7*, 1900595.
- (19) Feng, L.; Huo, P.; Liang, Y.; Xu, T. Photonic Metamaterial Absorbers: Morphology Engineering and Interdisciplinary Applications. *Adv. Mater.* **2020**, *32*, 1903787.
- (20) Bagheri, S.; Strohfeldt, N.; Sterl, F.; Berrier, A.; Tittl, A.; Giessen, H. Large-Area Low-Cost Plasmonic Perfect Absorber Chemical Sensor Fabricated by Laser Interference Lithography. ACS Sens. 2016, 1, 1148–1154.
- (21) Bhattarai, K.; Ku, Z.; Silva, S.; Jeon, J.; Kim, J. O.; Lee, S. J.; Urbas, A.; Zhou, J. A Large-Area, Mushroom-Capped Plasmonic Perfect Absorber: Refractive Index Sensing and Fabry-Perot Cavity Mechanism. *Adv. Opt. Mater.* **2015**, *3*, 1779–1786.

- (22) Amiri, M.; Tofigh, F.; Shariati, N.; Lipman, J.; Abolhasan, M. Wide-angle metamaterial absorber with highly insensitive absorption for TE and TM modes. *Sci. Rep.* **2020**, *10*, 13638.
- (23) Kim, J.; Seong, J.; Kim, W.; Lee, G.-Y.; Kim, S.; Kim, H.; Moon, S.-W.; Oh, D. K.; Yang, Y.; Park, J.; Jang, J.; Kim, Y.; Jeong, M.; Park, C.; Choi, H.; Jeon, G.; Lee, K.-i.; Yoon, D. H.; Park, N.; Lee, B.; et al. Scalable manufacturing of high-index atomic layer-polymer hybrid metasurfaces for metaphotonics in the visible. *Nat. Mater.* **2023**, 22, 474–481.
- (24) Qiu, Q.; Huang, Z. Photodetectors of 2D materials from ultraviolet to terahertz waves. *Adv. Mater.* **2021**, *33*, 2008126.
- (25) Sakotic, Z., Ware, A., Povinelli, M., Wasserman, D. Perfect Absorption at the Ultimate Thickness Limit in Planar Films. *ACS Photonics* **2023**, DOI: 10.1021/acsphotonics.3c01017.
- (26) Rozin, M. J.; Rosen, D. A.; Dill, T. J.; Tao, A. R. Colloidal metasurfaces displaying near-ideal and tunable light absorbance in the infrared. *Nat. Commun.* **2015**, *6*, 7325.
- (27) Shi, Q.; Connell, T. U.; Xiao, Q.; Chesman, A. S. R.; Cheng, W.; Roberts, A.; Davis, T. J.; Gómez, D. E. Plasmene Metasurface Absorbers: Electromagnetic Hot Spots and Hot Carriers. *ACS Photonics* **2019**, *6*, 314–321.
- (28) Wang, K.; Park, S. H.; Zhu, J.; Kim, J. K.; Zhang, L.; Yi, G.-R. Self-Assembled Colloidal Nanopatterns toward Unnatural Optical Meta-Materials. *Adv. Funct. Mater.* **2021**, *31*, 2008246.
- (29) Bonin, G. O.; Barrow, S. J.; Connell, T. U.; Roberts, A.; Chesman, A. S. R.; Gómez, D. E. Self-Assembly of Plasmonic Near-Perfect Absorbers of Light: The Effect of Particle Size. *J. Phys. Chem. Lett.* **2020**, *11*, 8378–8385.
- (30) Law, S.; Podolskiy, V.; Wasserman, D. Towards nano-scale photonics with micro-scale photons: the opportunities and challenges of mid-infrared plasmonics. *Nanophotonics* **2013**, *2*, 103–130.
- (31) Mueller, N. S.; Pfitzner, E.; Okamura, Y.; Gordeev, G.; Kusch, P.; Lange, H.; Heberle, J.; Schulz, F.; Reich, S. Surface-Enhanced Raman Scattering and Surface-Enhanced Infrared Absorption by Plasmon Polaritons in Three-Dimensional Nanoparticle Supercrystals. *ACS Nano* **2021**, *15*, 5523–5533.
- (32) Arul, R.; Grys, D.-B.; Chikkaraddy, R.; Mueller, N. S.; Xomalis, A.; Miele, E.; Euser, T. G.; Baumberg, J. J. Giant mid-IR resonant coupling to molecular vibrations in sub-nm gaps of plasmonic multilayer metafilms. *Light Sci. Appl.* **2022**, *11*, 281.
- (33) Jansons, A. W.; Hutchison, J. E. Continuous Growth of Metal Oxide Nanocrystals: Enhanced Control of Nanocrystal Size and Radial Dopant Distribution. ACS Nano 2016, 10, 6942–6951.
- (34) Agrawal, A.; Cho, S. H.; Zandi, O.; Ghosh, S.; Johns, R. W.; Milliron, D. J. Localized Surface Plasmon Resonance in Semi-conductor Nanocrystals. *Chem. Rev.* **2018**, *118*, 3121–3207.
- (35) Cho, S. H.; Roccapriore, K. M.; Dass, C. K.; Ghosh, S.; Choi, J.; Noh, J.; Reimnitz, L. C.; Heo, S.; Kim, K.; Xie, K.; Korgel, B. A.; Li, X.; Hendrickson, J. R.; Hachtel, J. A.; Milliron, D. J. Spectrally tunable infrared plasmonic F,Sn: In_2O_3 nanocrystal cubes. *J. Chem. Phys.* **2020**, 152, 014709.
- (36) Guo, Q.; Cui, Y.; Yao, Y.; Ye, Y.; Yang, Y.; Liu, X.; Zhang, S.; Liu, X.; Qiu, J.; Hosono, H. A Solution-Processed Ultrafast Optical Switch Based on a Nanostructured Epsilon-Near-Zero Medium. *Adv. Mater.* **2017**, *29*, 1700754.
- (37) Guo, Q.; Qin, Z.; Wang, Z.; Weng, Y.-X.; Liu, X.; Xie, G.; Qiu, J. Broadly Tunable Plasmons in Doped Oxide Nanoparticles for Ultrafast and Broadband Mid-Infrared All-Optical Switching. *ACS Nano* **2018**, *12*, 12770–12777.
- (38) Jiang, H.; Zhao, Y.; Ma, H.; Wu, Y.; Chen, M.; Wang, M.; Zhang, W.; Peng, Y.; Leng, Y.; Cao, Z.; Shao, J. Broad-Band Ultrafast All-Optical Switching Based on Enhanced Nonlinear Absorption in Corrugated Indium Tin Oxide Films. *ACS Nano* **2022**, *16*, 12878–12888.
- (39) Agrawal, A.; Singh, A.; Yazdi, S.; Singh, A.; Ong, G. K.; Bustillo, K.; Johns, R. W.; Ringe, E.; Milliron, D. J. Resonant Coupling between Molecular Vibrations and Localized Surface Plasmon Resonance of Faceted Metal Oxide Nanocrystals. *Nano Lett.* **2017**, *17*, 2611–2620.

- (40) Sun, K.; Riedel, C. A.; Wang, Y.; Urbani, A.; Simeoni, M.; Mengali, S.; Zalkovskij, M.; Bilenberg, B.; de Groot, C. H.; Muskens, O. L. Metasurface Optical Solar Reflectors Using AZO Transparent Conducting Oxides for Radiative Cooling of Spacecraft. *ACS Photonics* **2018**, *5*, 495–501.
- (41) Kim, K.; Sherman, Z. M.; Cleri, A.; Chang, W. J.; Maria, J.-P.; Truskett, T. M.; Milliron, D. J. Hierarchically Doped Plasmonic Nanocrystal Metamaterials. *Nano Lett.* **2023**, 23, 7633–7641.
- (42) Salisbury, W. W. Absorbent body for electromagnetic waves. US Patent US2599944A1952.
- (43) Fante, R. L.; McCormack, M. T. Reflection properties of the Salisbury screen. *IEEE Trans. Antennas Propag.* **1988**, *36*, 1443–1454.
- (44) Pozar, D. M. Microwave engineering; John Wiley & Sons, 2011.
- (45) Li, Y.; Heinz, T. F. Two-dimensional models for the optical response of thin films. 2D Mater. 2018, 5, 025021.
- (46) Sherman, Z. M.; Kim, K.; Kang, J.; Roman, B. J.; Crory, H. S. N.; Conrad, D. L.; Valenzuela, S. A.; Lin, E.; Dominguez, M. N.; Gibbs, S. L.; Anslyn, E. V.; Milliron, D. J.; Truskett, T. M. Plasmonic Response of Complex Nanoparticle Assemblies. *Nano Lett.* **2023**, 23, 3030–3037.
- (47) Akselrod, G. M.; Huang, J.; Hoang, T. B.; Bowen, P. T.; Su, L.; Smith, D. R.; Mikkelsen, M. H. Large-Area Metasurface Perfect Absorbers from Visible to Near-Infrared. *Adv. Mater.* **2015**, 27, 8028–8034
- (48) Vieira, B. G. M.; Mueller, N. S.; Barros, E. B.; Reich, S. Plasmonic Properties of Close-Packed Metallic Nanoparticle Monoand Bilayers. *J. Phys. Chem. C* **2019**, *123*, 17951–17960.
- (49) Mack, D. L.; Cortés, E.; Giannini, V.; Török, P.; Roschuk, T.; Maier, S. A. Decoupling absorption and emission processes in superresolution localization of emitters in a plasmonic hotspot. *Nature Commun.* **2017**, *8*, 14513.
- (50) ElKabbash, M.; Sreekanth, K. V.; Alapan, Y.; Kim, M.; Cole, J.; Fraiwan, A.; Letsou, T.; Li, Y.; Guo, C.; Sankaran, R. M.; Gurkan, U. A.; Hinczewski, M.; Strangi, G. Hydrogen sensing using thin-film perfect light absorber. *ACS Photonics* **2019**, *6*, 1889–1894.
- (51) Törmä, P.; Barnes, W. L. Strong coupling between surface plasmon polaritons and emitters: a review. *Rep. Prog. Phys.* **2015**, *78*, 013901.
- (52) Hertzog, M.; Wang, M.; Mony, J.; Börjesson, K. Strong light-matter interactions: a new direction within chemistry. *Chem. Soc. Rev.* **2019**, *48*, 937–961.
- (53) Piper, J. R.; Fan, S. Total absorption in a graphene monolayer in the optical regime by critical coupling with a photonic crystal guided resonance. *ACS Photonics* **2014**, *1*, 347–353.
- (54) Canales, A.; Kotov, O.; Shegai, T. O. Perfect Absorption and Strong Coupling in Supported MoS₂ Multilayers. *ACS Nano* **2023**, *17*, 3401–3411.
- (55) Staller, C. M.; Gibbs, S. L.; Cabezas, C. A. S.; Milliron, D. J. Quantitative Analysis of Extinction Coefficients of Tin-Doped Indium Oxide Nanocrystal Ensembles. *Nano Lett.* **2019**, *19*, 8149–8154.
- (56) Gibbs, S. L.; Staller, C. M.; Agrawal, A.; Johns, R. W.; Saez Cabezas, C. A.; Milliron, D. J. Intrinsic Optical and Electronic Properties from Quantitative Analysis of Plasmonic Semiconductor Nanocrystal Ensemble Optical Extinction. *J. Phys. Chem. C* **2020**, *124*, 24351–24360.
- (57) Tandon, B.; Agrawal, A.; Heo, S.; Milliron, D. J. Competition between depletion effects and coupling in the plasmon modulation of doped metal oxide nanocrystals. *Nano Lett.* **2019**, *19*, 2012–2019.
- (58) Mayerhöfer, T. G.; Popp, J. Quantitative Evaluation of Infrared Absorbance Spectra Lorentz Profile versus Lorentz Oscillator. *ChemPhysChem* **2019**, *20*, 31–36.
- (59) Paggi, L.; Fabas, A.; El Ouazzani, H.; Hugonin, J.-P.; Fayard, N.; Bardou, N.; Dupuis, C.; Greffet, J.-J.; Bouchon, P. Over-coupled resonator for broadband surface enhanced infrared absorption (SEIRA). *Nat. Commun.* **2023**, *14*, 4814.
- (60) Shi, X.; Ueno, K.; Oshikiri, T.; Sun, Q.; Sasaki, K.; Misawa, H. Enhanced water splitting under modal strong coupling conditions. *Nat. Nanotechnol.* **2018**, *13*, 953–958.

- (61) Vassant, S.; Hugonin, J.-P.; Marquier, F.; Greffet, J.-J. Berreman mode and epsilon near zero mode. *Opt. Express* **2012**, *20*, 23971–23977.
- (62) Hsu, A. L.; Herring, P. K.; Gabor, N. M.; Ha, S.; Shin, Y. C.; Song, Y.; Chin, M.; Dubey, M.; Chandrakasan, A. P.; Kong, J.; Jarillo-Herrero, P.; Palacios, T. Graphene-Based Thermopile for Thermal Imaging Applications. *Nano Lett.* **2015**, *15*, 7211–7216.
- (63) Zhang, C.; Yang, J.; Li, Y.; Song, J.; Guo, J.; Fang, Y.; Yang, X.; Yang, Q.; Wang, D.; Deng, X. Vapor-Liquid Transition-Based Broadband Light Modulation for Self-Adaptive Thermal Management. *Adv. Funct. Mater.* **2022**, 32, 2208144.
- (64) Tang, X.; Ackerman, M. M.; Shen, G.; Guyot-Sionnest, P. Towards infrared electronic eyes: flexible colloidal quantum dot photovoltaic detectors enhanced by resonant cavity. *Small* **2019**, *15*, 1804920.
- (65) Dang, T. H.; Abadie, C.; Khalili, A.; Greboval, C.; Zhang, H.; Prado, Y.; Xu, X. Z.; Gacemi, D.; Descamps-Mandine, A.; Ithurria, S.; Todorov, Y.; Sirtori, C.; Vasanelli, A.; Lhuillier, E. Broadband Enhancement of Mid-Wave Infrared Absorption in a Multi-Resonant Nanocrystal-Based Device. *Adv. Opt. Mater.* **2022**, *10*, 2200297.
- (66) Yang, Y.; Lu, J.; Manjavacas, A.; Luk, T. S.; Liu, H.; Kelley, K.; Maria, J.-P.; Runnerstrom, E. L.; Sinclair, M. B.; Ghimire, S.; Brener, I. High-harmonic generation from an epsilon-near-zero material. *Nat. Phys.* **2019**, *15*, 1022–1026.
- (67) A. S., A.; O'Donnell, C. F.; Chaitanya Kumar, S.; Ebrahim-Zadeh, M.; Tidemand-Lichtenberg, P.; Pedersen, C. Mid-infrared upconversion imaging using femtosecond pulses. *Photonics Res.* **2019**, 7, 783–791.
- (68) Gorlach, A.; Neufeld, O.; Rivera, N.; Cohen, O.; Kaminer, I. The quantum-optical nature of high harmonic generation. *Nature Commun.* **2020**, *11*, 4598.
- (69) Hui, Y.; Gomez-Diaz, J. S.; Qian, Z.; Alu, A.; Rinaldi, M. Plasmonic piezoelectric nanomechanical resonator for spectrally selective infrared sensing. *Nat. Commun.* **2016**, *7*, 11249.
- (70) Lee, D.; Go, M.; Kim, M.; Jang, J.; Choi, C.; Kim, J. K.; Rho, J. Multiple-patterning colloidal lithography-implemented scalable manufacturing of heat-tolerant titanium nitride broadband absorbers in the visible to near-infrared. *Microsyst. Nanoeng.* **2021**, *7*, 14.
- (71) Li, D.; Liu, X.; Li, W.; Lin, Z.; Zhu, B.; Li, Z.; Li, J.; Li, B.; Fan, S.; Xie, J.; Zhu, J. Scalable and hierarchically designed polymer film as a selective thermal emitter for high-performance all-day radiative cooling. *Nat. Nanotechnol.* **2021**, *16*, 153–158.
- (72) Zandi, O.; Agrawal, A.; Shearer, A. B.; Reimnitz, L. C.; Dahlman, C. J.; Staller, C. M.; Milliron, D. J. Impacts of surface depletion on the plasmonic properties of doped semiconductor nanocrystals. *Nat. Mater.* **2018**, *17*, 710–717.
- (73) Giannuzzi, R.; De Donato, F.; De Trizio, L.; Monteduro, A. G.; Maruccio, G.; Scarfiello, R.; Qualtieri, A.; Manna, L. Tunable Near-Infrared Localized Surface Plasmon Resonance of F, In-Codoped CdO Nanocrystals. ACS Appl. Mater. Interfaces 2019, 11, 39921–30020
- (74) Chang, W. J.; Sakotic, Z.; Ware, A.; Green, A. M.; Roman, B. J.; Kim, K.; Truskett, T. M.; Wasserman, D.; Milliron, D. J. Wavelength Tunable Infrared Perfect Absorption in Plasmonic Nanocrystal Monolayers. *ChemRxiv* **2023**, No. 2023-jhhm2v1, DOI: 10.26434/chemrxiv-2023-jhhm2.